


# Better and Faster Velocity Pulsatility Assessment in Cerebral White Matter Perforating Arteries With 7T Quantitative Flow MRI Through Improved Slice Profile, Acquisition Scheme, and Postprocessing

Lennart Geurts <sup>1\*</sup>, Geert Jan Biessels,<sup>2</sup> Peter Luijten,<sup>1</sup> and Jaco Zwanenburg<sup>1</sup>

**Purpose:** A previously published cardiac-gated 2D Qflow protocol at 7T in cerebral perforating arteries was optimized to reduce velocity underestimation and improve temporal resolution.

**Methods:** First, the signal-to-noise ratio (SNR) gain of the velocity measurement ( $SNR_v$ ) was tested for two signal averages versus one. Second, the decrease in velocity underestimation with a tilted optimized nonsaturating excitation (TONE) pulse was tested. Third, the decrease in pulsatility index (PI) underestimation through improved temporal resolution was tested. Test-retest agreement was measured for the resulting acquisition in older volunteers (mean age 63 years), and the results were compared with the other volunteers (mean age 26 years).

**Results:** Using two signal averages increased  $SNR_v$  by only 12% ( $P=0.04$ ), probably due to motion of the subvoxel-size arteries. The TONE decreased velocity underestimation, thereby increasing the mean velocity from 0.52 to 0.67 cm/s ( $P < 0.001$ ). The PI increased substantially with increasing temporal resolution. The test-retest agreement showed good coefficients of repeatability of 0.18 cm/s for velocity and 0.14 for PI. The measured velocity was lower in the older group: 0.42 versus 0.51 cm/s ( $P=0.05$ ).

**Conclusions:** The optimized sequence yields better velocity and PI estimates in small vessels, has twice as good test-retest agreement, and has a suitable scan time for use in patients.

**Magn Reson Med 79:1473–1482, 2018. © 2017 The Authors Magnetic Resonance in Medicine published by Wiley Periodicals, Inc. on behalf of International Society for Magnetic Resonance in Medicine. This is an open access article under the terms of the Creative Commons Attribution-NonCommercial License, which permits use, distribution and reproduction in any medium, provided the original work is properly cited and is not used for commercial purposes.**

**Key words:** brain; MRI; blood; flow; velocity; pulsatility

## INTRODUCTION

Advances in ultrahigh-field MRI have led to new methods to measure the structure and function of cerebral small vessels. Measuring the function of cerebral small vessels can make a significant contribution to our understanding of the physiology of cerebral microcirculation, as well as its diseases. Moreover, it may also be of use to test the effects of pharmacological agents. Cerebral small vessel disease (SVD) is one of such diseases for which more advanced assessment of small vessel function is needed. Small vessel disease is involved in approximately half of all dementias (1–3) and up to a quarter (4–9) of all strokes. Yet, its underlying mechanisms are poorly understood, as measuring the *in vivo* function of these small vessels was not possible until recently. Last year, we published a cardiac-gated 2D phase-contrast method with 7T MRI capable of measuring blood flow velocity and its pulsatility in cerebral perforating arteries of the semi-oval center (CSO, the white matter found underneath the gray matter on the surface of the brain). The method measures blood-flow velocity in the perforators of the CSO reproducibly (10). However, the 2D phase-contrast quantitative flow (2D Qflow) scan can potentially be further optimized for the properties of these tiny vessels.

First, there is a substantial partial-volume effect because of the small diameters of the CSO perforators. This leads to an underestimation of the blood flow velocity, with a measured velocity in the range of 0.5 to 1.0 cm/s in white matter perforating arteries (10). Although there is no reference standard available to measure flow in these very small arteries in human cerebral white matter, laser Doppler measurements in similarly sized retinal arterioles (with diameters of approximately 116  $\mu\text{m}$ ) show blood flow velocities between 2.0 and 4.0 cm/s (11). To address this underestimation, we hypothesized that applying a tilted optimized nonsaturating excitation (TONE) pulse will decrease the saturation of blood spins along the imaging slice and, thus, the velocity underestimation (12). Tilting the flip angle along the excited slice decreases blood saturation at the inflow side, whereas blood signal at the outflow side is increased. TONE has been used extensively to reduce

<sup>1</sup>UMC Utrecht, Department of Radiology, Utrecht, the Netherlands.

<sup>2</sup>UMC Utrecht, Brain Centre Rudolf Magnus, Department of Neurology, Utrecht, the Netherlands.

This research received funding from the European Research Council under the European Union's Seventh Framework Programme (FP/2007-2013)/ERC Grant Agreement No. 337333.

\*Correspondence to: Lennart Geurts, M.D., UMC Utrecht, Department of Radiology, Postbus 85500, 3508 GA, Utrecht, the Netherlands. E-mail: l.j.geurts-2@umcutrecht.nl

Correction added after online publication 24 August 2017. The affiliation for Geert Jan Biessels has been corrected.

Received 4 January 2017; revised 24 May 2017; accepted 11 June 2017  
DOI 10.1002/mrm.26821

Published online 11 July 2017 in Wiley Online Library (wileyonlinelibrary.com).  
© 2017 The Authors Magnetic Resonance in Medicine published by Wiley Periodicals, Inc. on behalf of International Society for Magnetic Resonance in Medicine. This is an open access article under the terms of the Creative Commons Attribution-NonCommercial License, which permits use, distribution and reproduction in any medium, provided the original work is properly cited and is not used for commercial purposes.

blood saturation in multislab acquisitions of the large vessels (13). Although the saturation of blood in large vessels is only a problem in thick excitation slabs because of high blood-flow velocity, the slow-flowing blood in small vessels causes saturation to be relevant at much thinner excitation widths. Increasing the amount of blood signal decreases the partial volume effect and thereby the underestimation of velocity and pulsatility.

Second, the temporal resolution of 160 ms could be considered low, potentially underestimating pulsatility. The appropriate temporal resolution for small vessels depends on their physiological velocity time curve (14). For large vessels, a minimal temporal resolution of 40 ms has been suggested, to accurately measure the peak velocity (14). The true waveform at the level of the small vessels can only be assessed with a sufficiently high temporal resolution. To address the underestimation of pulsatility by a limited temporal resolution, we aimed to investigate the effect of temporal resolution on the estimated pulsatility index.

Finally, because of the long scan time of 6 to 7 min, subject motion can be relatively large compared with the subvoxel dimensions of the imaged vessels. If motion leads to a shift of the subvoxel perforator to the neighboring voxel, there is effectively no averaging taking place. This increased sensitivity to subject motion may cause suboptimal gains in the signal-to-noise ratio (SNR) from signal averaging, as the small vessels are spread over multiple voxels rather than averaged. To address the efficiency of scan time, we aimed to assess the gain obtained by averaging. The results show that this is less than the traditional square-root law, presumably the result of motion of the subvoxel vessels to neighboring voxels.

The main goal of this work is to create a cardiac-gated 2D Qflow protocol that has less underestimation for small-vessel velocity measurements, has a temporal resolution suitable for small-vessel waveforms, and makes efficient use of scan time. The averaging effect was tested first, after which all other measurements were performed without averaging. This yielded a scan time to do a repeated measurement with and without a TONE pulse or with increased temporal resolution. Simulation of blood saturation with and without TONE was used to show its theoretical benefit. The waveform of the acquisition with the highest temporal resolution was used to simulate the effect of limited temporal resolution. Based on these results, we provide a recommendation for a protocol with the least underestimation of velocity and pulsatility within a practical scan time. Finally, to assess the applicability in older subjects, the test-retest agreement of the recommended protocol was assessed in an older group of volunteers.

## METHODS

The previously published 2D Qflow acquisition for cerebral perforating arteries was modified, and the effect of these modifications was tested in three experiments (10). Each experiment started with the optimal acquisition, as concluded from the previous experiment. The first experiment assessed the effect of reducing the number of

signal averages (NSA) on the SNR. Limited loss in SNR upon a reduction in NSA might allow to reduce scan time, to accommodate further improvements. The second experiment assessed the effect of TONE on velocity and pulsatility underestimation. Simulation of blood saturation with a sinc-Gauss pulse and with a TONE pulse was used to show the theoretical benefit. The third and final experiment assessed the effect of temporal resolution on pulsatility underestimation. The waveform of the acquisition with the highest temporal resolution was used to simulate the effect of reduced temporal resolution. Each of the three aspects was tested separately in groups of eight young and healthy volunteers. In addition, the test-retest agreement was assessed in eight older and healthy volunteers.

## Measurements

This study was approved by the institutional review board of our institution, and all subjects provided written informed consent. All acquisitions were performed on a 7T Philips Achieva MRI system (Philips Healthcare, Best, the Netherlands) with a 32-channel receive coil with volume transmit/receive coil for transmission (Nova Medical, Wilmington, MA). Each of the three experiments was performed on eight healthy volunteers. A peripheral pulse unit was used for gating of the retrospectively gated 2D Qflow acquisitions. The 2D Qflow slice was planned through the CSO, the white matter core underneath the gray matter on the brain's surface. To achieve this, the slice was planned parallel to the plane through the genu and splenium of the corpus callosum and 15 mm above its top. If a 2D Qflow acquisition already showed obvious motion artifacts during scanning, then it was immediately repeated without replanning. For every experiment, the specific version of the 2D Qflow acquisition was alternated with a fast T<sub>1</sub>-weighted 3D turbo field-echo (TFE) acquisition for white matter segmentation. Figure 1 shows the slice planning and an example of a 2D Qflow slice. All 2D Qflow acquisitions had an anterior–posterior phase-encoding direction, which appeared to be less sensitive to ghosting artifacts through the CSO from leptomeningeal arteries, compared with the right–left phase-encoding direction (as used in the previously published version) (10). The field of view in the phase-encoding direction increased from 180 to 250 mm, whereas the SENSE factor increased from 1 to 1.5, to keep the scan time and SNR approximately equal to the published version. Thus, all 2D Qflow acquisitions had a 250 × 250 mm<sup>2</sup> field of view, a 0.3 × 0.3 × 2.0 mm<sup>3</sup> acquired voxel size (reconstructed to 0.2 × 0.2 × 2.0 mm<sup>3</sup>), an acquired time fraction of 0.5 (i.e., reconstruction was interpolated with a factor of 2 in the time dimension) and an encoding velocity ( $V_{\text{enc}}$ ) of 4 cm/s.

The parameters that were adjusted for the three experiments are displayed in Table 1. To test the effect of signal averaging on SNR and perforator detection, two NSA = 1 repeats of the original 2D Qflow acquisition were acquired. The magnitude and velocity map were converted to complex values, and the two NSA = 1 repeats were combined to create the NSA = 2 image. To test the effect of applying a TONE pulse on velocity

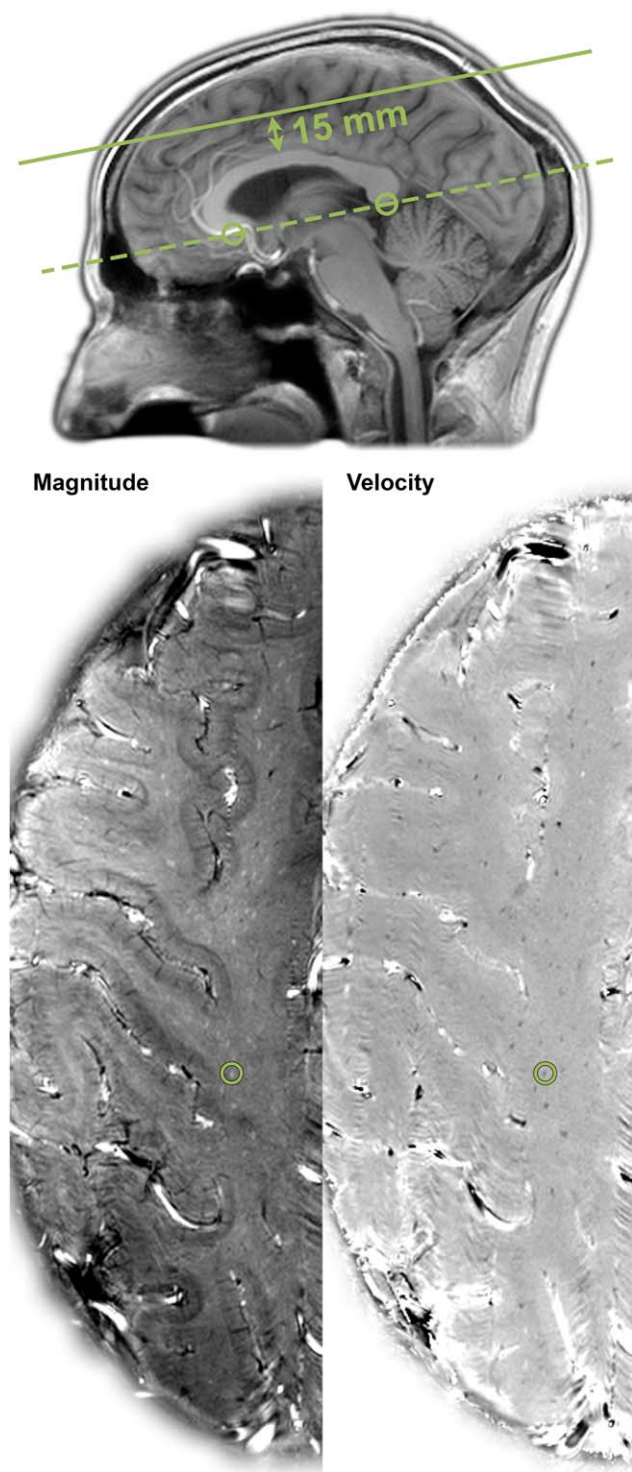


FIG. 1. Slice planning. The top image shows the planning of the 2D Qflow slice on the  $T_1$ -weighted volume. The dashed line shows the orientation of the slice, parallel to the corpus callosum. After aligning the orientation, the slice is planned 1.5 cm above the top of the corpus callosum as indicated by the solid line. The bottom images show the magnitude and velocity (mean over all cardiac time points) of the planned 2D Qflow slice, with one detected perforating artery marked with a green circle as an example.

underestimation, the NSA = 1 acquisition was acquired with the default radiofrequency (RF) pulse (flip angle =  $60^\circ$ ) and with TONE (flip angle =  $50$ – $90^\circ$ ). For the TONE pulse, the implementation of the vendor was used. The default RF pulse was an asymmetric sinc-Gauss pulse with one lobe and is referred to as the sinc pulse in the remainder of the text and figures. To test the effect of temporal resolution on pulsatility index (PI) underestimation, the TONE acquisition was acquired with a TFE factor of 3, 2, and 1. As illustrated in Figure 2, the TFE factor is defined as the number of phase-contrast-encoding cycles (positive and negative bipolar velocity encoding per k-line) per cardiac time point. A TFE factor of 1 yields the longest scan duration, but with the highest temporal resolution, whereas a cardiac time point has the duration of one phase-contrast-encoding cycle (which equals two repetition times (TRs)). Finally, the test-retest agreement of the TFE = 2 acquisition was assessed in a group of older volunteers. The acquisition was performed twice in succession without replanning, reflecting imprecision caused by thermal and physiological noise. The acquisition was performed a third time with replanning after the volunteers were briefly taken out of the scanner and repositioned in the scanner, reflecting imprecision caused by slice planning.

#### Image Processing

Image processing was identical for all three experiments. A MATLAB (version R2015b, the MathWorks, Natick, MA) tool that was developed in house was used to process the acquired images and automatically detect perforators. Therefore, no manual selection of CSO perforators or white matter was necessary—an improvement over the previously published method. The tool performed the following steps:

1. White matter segmentation. The  $T_1$ -weighted data set acquired closest in time (before or after) the 2D Qflow was used to segment the white matter using SPM12 functions (Wellcome Trust Centre for Neuroimaging) (15). The segmentation probability map was transformed to the image space of the 2D Qflow and converted to a mask (threshold probability 0.95) so that it only contained white matter.
2. Background phase correction in the velocity maps. The mean velocity of tissue has to be 0 cm/s. The mean velocity map (mean over the cardiac cycle) was median filtered with a  $10 \times 10 \text{ mm}^2$  kernel ( $50 \times 50$  pixels) and subtracted from the velocity map of each cardiac time point. Because the density of visible white matter perforating the arteries is low, the median filter removes those CSO perforators in the calculation of the mean background velocity.
3. Estimation of the SNR of the velocity map ( $\text{SNR}_v$ ). The magnitude and velocity map were converted to complex data. The standard deviations over cardiac time points was computed for the real and imaginary part, and the root mean square of these standard deviations was subsequently median filtered with a  $10 \times 10 \text{ mm}^2$  kernel ( $50 \times 50$  pixels). This resulted in the estimated standard deviation of the noise in the magnitude,



Table 1  
Scan Parameters for the Different 2D Qflow Versions for Each of the Three Experiments.

Experiment	NSA	TONE	Temporal resolution
NSA	<b>2</b>	<b>1</b>	1
RF pulse	Sinc	<b>Sinc</b>	TONE
TFE factor	3	3	<b>2</b>
Flip angle (°)	60	60	50–90
TR/TE (ms)	26/16	26/16	28/16
BW (Hz/pix)	59	59	59
Temporal resolution (ms)	159	159	114
Reconstructed time points	10	10	15
Scan time (min:sec)	5:20	2:40	4:15

Note: The scan time and reconstructed time points are for a heart rate of 62 bpm.

which was used to calculate the SNR of the magnitude images ( $SNR_{mag}$ ). The standard deviation (SD) of noise in the velocity ( $SD_v$ ) was calculated with Equation [1]. Although this SNR estimation is not perfect (as it includes physiological noise, and not only the thermal noise), it is an effective way to consistently select vessels with significant flow.

$$SD_v = \frac{V_{enc}}{\pi} \frac{1}{SNR_{mag}}. \quad [1]$$

4. Estimation of confidence intervals for mean velocity ( $V_{mean}$ ). The  $V_{mean}$  was computed as the mean velocity over the cardiac cycle after the background phase correction of step 2. Statistical significance ( $\alpha$ ) was set to 0.05, and was Bonferroni corrected for repeated testing by dividing it by the number of acquired voxels in the CSO mask ( $\alpha_{corr}$ ). The inverse normal cumulative distribution function was used with  $V_{mean}$  and  $SD_v$  to calculate the two-sided 95% confidence interval (95% CI) for  $V_{mean}$  (between  $\alpha_{corr}/2$  and  $1-\alpha_{corr}/2$ ).
5. Identification of cerebral perforating arteries based on significant  $V_{mean}$ . All voxels inside the CSO mask that did not contain 0 zero cm/s within their 95% CI of  $V_{mean}$  were considered significant. Every group of adjacent significant voxels was considered belonging to one perforator. Because CSO perforators are known to flow downward, only groups with negative  $V_{mean}$  were included. Because perforators have subvoxel diameters, for every group the voxel with the highest absolute  $V_{mean}$  was identified as the perforator.
6. Optional matching between two separate acquisitions. If matching was performed, the CSO perforators that were not detected in both acquisitions were discarded. Perforators were regarded to match if the mean flow was significant in both acquisitions, and if they were the closest possible match within 2-mm distance.
7. Velocity time curve extraction and PI calculation. The velocity curve was extracted from the data for each voxel identified as a perforator. These time curves were combined to create the average time curve of the perforators. The PI was calculated from this average time curve as follows:

$$PI = \frac{|V|_{max} - |V|_{min}}{|V|_{mean}} \quad [2]$$

## Analysis

After image processing, the number of detected perforators ( $N_{detected}$ ),  $V_{mean}$ ,  $SNR_v$  ( $V_{mean}/SD_v$ ), and PI were recorded. These parameters were available for the average time curve of all detected perforators or for that of matched perforators only. For each experiment, the parameters that were hypothesized to be primarily affected were tested between subsequent acquisitions

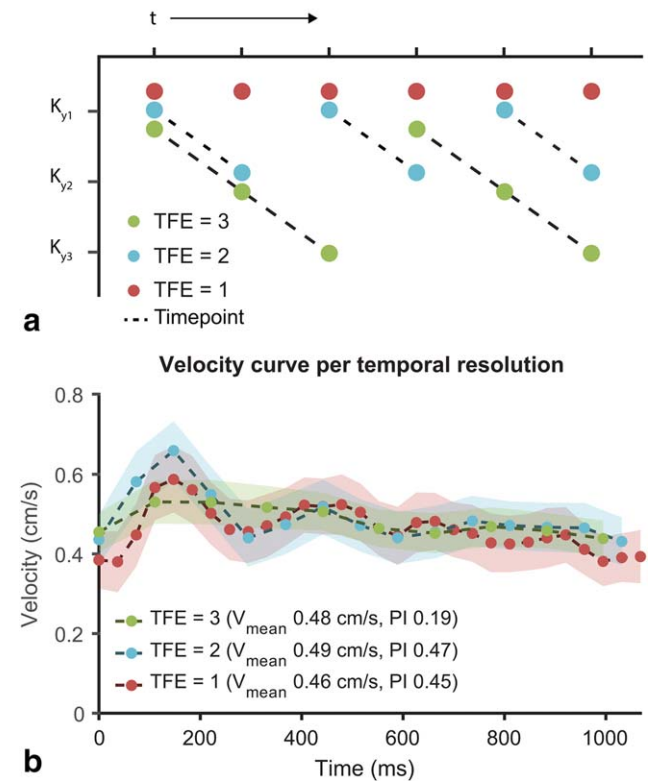


FIG. 2. Turbo field-echo factor definition. **a**: Difference in K-space acquisition scheme for the different TFE factors. The first 12 TRs (6 velocity encoding cycles) of an acquisition are shown in red, blue, and green for TFE=1, 2 and 3, respectively. With an increasing TFE factor, an increasing number of K-lines with different phase encoding are acquired within the same cardiac cycle. This leads to full K-space coverage in fewer cycles, but at the cost of acquiring fewer time points in one cycle. **b**: Acquired time curves for one volunteer, with different TFE factors.

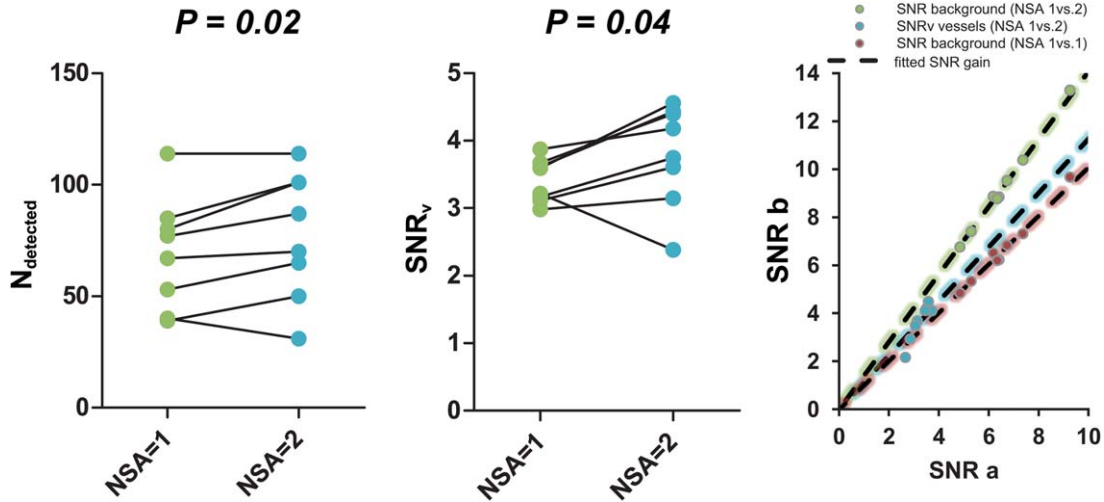


FIG. 3. NSA experiment results. In the left and center graphs, colored markers show individual measurements, and black lines show corresponding subjects. The  $P$  values are shown for the significant differences. The left graph shows the number of detected vessels. The center graph shows the  $\text{SNR}_v$  for matched vessels. In the right graph, colored markers show individual subjects and the dotted lines show the fitted SNR increase. The SNR increase is shown for the gain of interest (increased NSA effect for vessels, blue markers), theoretical gain (increased NSA effect for background, green markers), and no gain (repeated NSA=1 measurement for background, red markers). Note that the range of the SNR-b axis is  $\sqrt{2}$  larger than the range of the SNR-a axis.

(Table 1) using two sample t-tests (paired if testing matched perforators). All tests were performed single sided with an  $\alpha$  of 0.05. For the NSA experiment,  $\text{SNR}_v$  was tested to increase from the first repeat (NSA=1) to the combined repeats (NSA=2) for matched perforators only.  $N_{\text{detected}}$  was tested to increase between NSA=1 and NSA=2. For the TONE experiment, the  $\text{SNR}_v$ ,  $V_{\text{mean}}$ , and PI were tested to increase from the sinc pulse to TONE for matched perforators only.  $N_{\text{detected}}$  was tested to increase for unmatched perforators. For the temporal resolution experiment, PI was tested to increase for matched perforators.  $N_{\text{detected}}$  was tested to increase between the TFE factor=3 and 2 acquisitions, and between the TFE factor=2 and 1 acquisitions, because the longer acquisition increases the SNR of the average velocity map, and thereby increases the perforator detectability.

The first measurement of the test-retest experiment was compared with the second measurement (without repositioning), and the second measurement was compared with the third measurement (with repositioning) in Bland-Altman analyses. The coefficients of repeatability were calculated, the first reflecting system stability and the second including the effect of planning error as well. The difference in  $V_{\text{mean}}$ , PI, and  $N_{\text{detected}}$  between this group of older volunteers and the younger group with the same protocol from the TFE experiment was tested for significance, and the effect size was calculated (Cohen's  $d$ , mean difference divided by the pooled standard deviation).

### Simulations

Simulations were performed to support the interpretation of the results from the TONE and TFE experiments. The benefit of applying a TONE pulse to decrease blood-signal saturation was simulated using Monte Carlo simulation with the Bloch equations. The effect of temporal resolution and trigger delay on the measured PI was

simulated by resampling the average curve from the highest temporal resolution from the TFE experiment. We refer to the supplementary file for further details.

## RESULTS

### NSA Experiment

Scans were successfully completed in all eight subjects (mean age 32 (range, 21–38) years, 4 males, 4 females) of the NSA experiment. Figure 3 shows the results for the NSA experiment. The  $\text{SNR}_v$  in detected perforators increased with a factor of 1.12 (95% CI, 0.99–1.26) in the NSA=2 images compared with the NSA=1 images, whereas the SNR of the background increased with a factor of 1.41 (95% CI, 1.40–1.42). When comparing the background SNR between both NSA=1 scans, a factor of 0.99 [95% CI, 0.97–1.01] was found. Slightly more perforators were detected in the NSA=2 images compared with the NSA=1 images, with  $N_{\text{detected}}=77$  (range, 31–114) and 69 (range, 39–114) for NSA=2 and NSA=1, respectively ( $P=0.02$ , Fig. 3). Obviously, the scan time increased with a factor of 2 for NSA=2 relative to NSA=1 (from 2:40 to 5:20 min at 62 bpm, Table 1). For this reason, in the subsequent experiments only NSA=1 acquisitions were performed.

### TONE Experiment

Scans were successfully completed in all eight subjects of the TONE experiment. However, Subject 4 showed a large and opposite change in PI from the other subjects. Manual examination revealed that the sinc average time curve showed no pulse, which is physiologically unlikely and does not agree with the TONE average time curve. Further examination showed that this 2D Qflow slice was very close to gray matter in the sulci. This resulted in lower segmented white matter probabilities than usual, leading

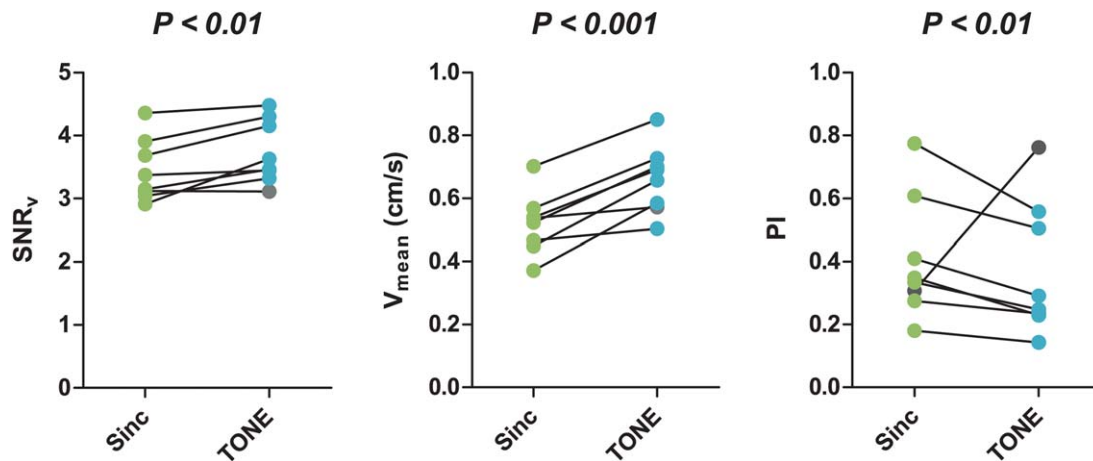


FIG. 4. TONE experiment results. Colored markers show individual measurements, and black lines show corresponding subjects. The outlier excluded from analysis is shown in gray. The  $P$  values are  $P < 0.01$  for the significant results. The left graph shows the  $SNR_v$ , the center graph shows  $V_{mean}$ , and the right graph shows PI.

to a conservative white matter mask. Post hoc analysis showed that the PI change in Subject 4 was an outlier according to Tukey's range test. For these reasons, Subject 4 was excluded from analysis (mean age after exclusion 27 (range, 23–31) years, 4 males, 3 females).

Using a TONE pulse significantly increased the  $V_{mean}$ ,  $SNR_v$ , and  $N_{detected}$  compared with the sinc acquisitions:  $V_{mean}$  ( $\pm$  standard error (SE)) increased from  $0.52 \pm 0.04$  to  $0.67 \pm 0.04$  cm/s ( $P < 0.001$ , Fig. 4),  $SNR_v$  ( $\pm$  SE) increased from  $3.5 \pm 0.20$  to  $3.8 \pm 0.18$  ( $P < 0.01$ , Fig. 4), and  $N_{detected}$  increased from 51 (range, 19–80) to 77 (range, 27–134) ( $P < 0.01$ ). The measured PI ( $\pm$  SE) decreased significantly from  $0.42 \pm 0.08$  to  $0.32 \pm 0.06$  ( $P < 0.01$ , Fig. 4). Using a TONE pulse increased the TR from 26 to 28 ms, which caused temporal resolution to worsen from 159 to 170 ms and caused the scan time to increase from 2:40 to 2:50 min. In the temporal

resolution experiment, only acquisitions with TONE excitation were performed.

#### Temporal Resolution Experiment

Scans were successfully completed in all eight subjects of the temporal resolution experiment. However, Subject 8 showed severe motion artifacts in all three acquisitions as a result of small posture and large freedom of motion, and was excluded from analysis (mean age after exclusion 26 (range, 23–30) years, 4 males, 3 females).

Figure 5 shows comparisons between acquisitions with different TFE factor settings. A significant increase in PI was observed for both changes in TFE factor ( $\pm$  SE), with  $0.28 \pm 0.03$  to  $0.43 \pm 0.02$  going from TFE factor=3 to 2 ( $P < 0.01$ ) and  $0.50 \pm 0.03$  to  $0.61 \pm 0.05$  from TFE factor=2 to 1 ( $P = 0.01$ ). There were no

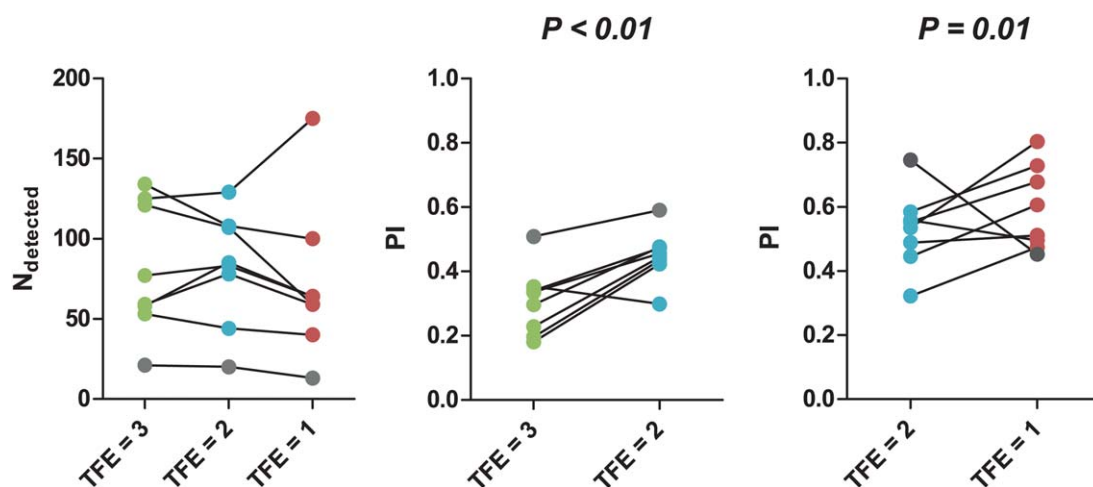
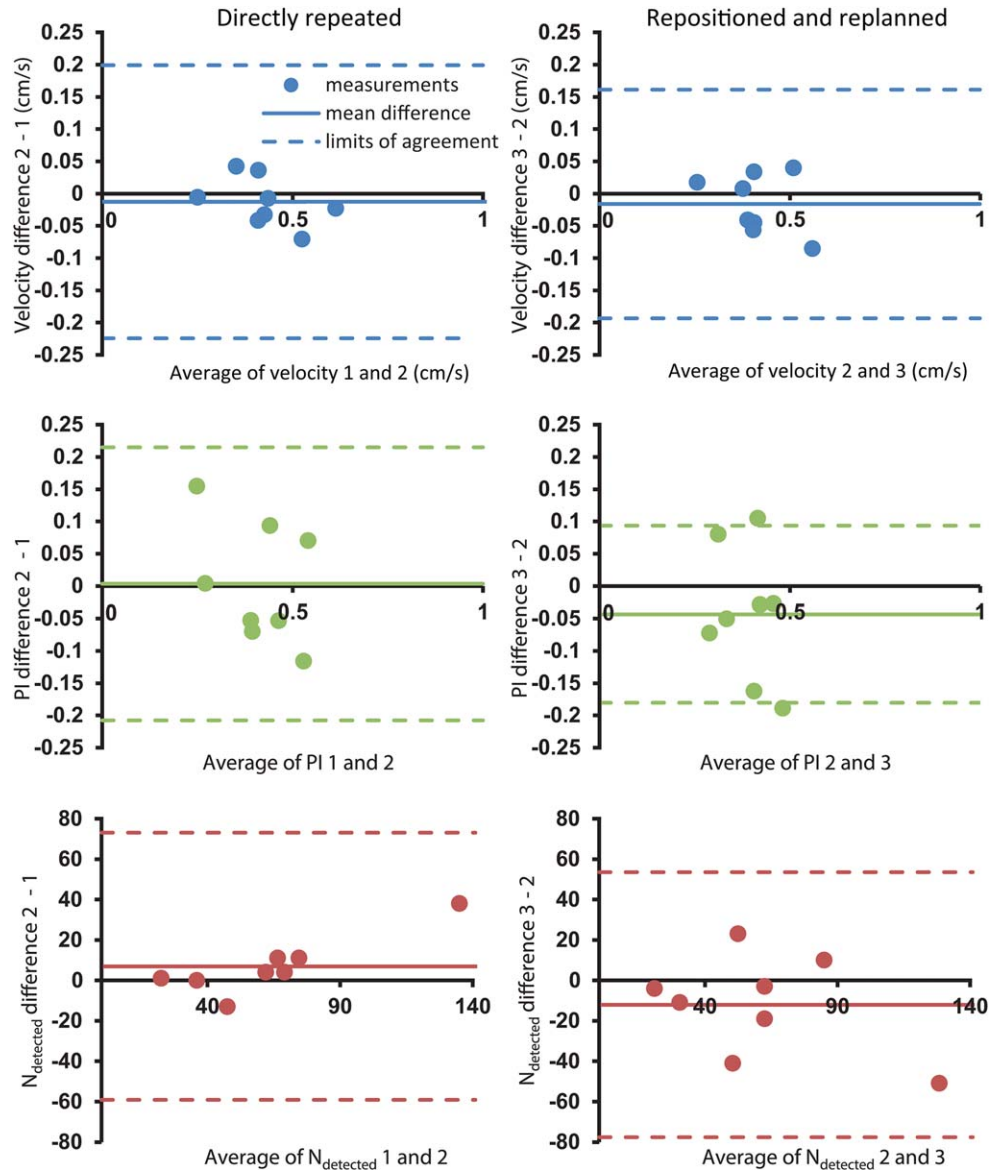


FIG. 5. Temporal resolution experiment results. Colored markers show individual measurements, and black lines show corresponding subjects. The  $P$  values are shown for the significant results. The left graph shows the number of detected vessels. The center and right graphs show the PI for matched vessels. In the center graph, TFE factor=3 and TFE factor=2 are compared; in the right graph, TFE factor=2 and TFE factor=1 are compared. The data points for TFE factor=2 are slightly different per plot, as the perforators for which the comparisons are made were matched between the two compared TFE factor images. The subject excluded from analysis as a result of severe motion artifacts is shown in gray.

FIG. 6. Bland-Altman plots for test-retest agreement in a group of eight older volunteers. The graphs show the difference between repeated measurements, plotted against the average of the repeated measures. The solid lines show the mean difference, and the dashed lines show the limits of agreement (mean difference  $\pm$  coefficient of repeatability). This is shown for the measured  $V_{\text{mean}}$  (the top graphs), PI (the center graphs), and  $N_{\text{detected}}$  (the bottom graphs). Measures were repeated with (right graphs) and without (left graphs) getting the subject out of the scanner, showing that test-retest agreement did not get worse with repositioning and replanning.



significant differences in  $N_{\text{detected}}$  between the acquisitions with a different TFE factor setting, with 90 (range, 53–134), 91 (range, 44–129), and 80 (range, 40–175) for TFE factor = 3, 2 and 1, respectively.

Scans were completed successfully in the eight older subjects of the test-retest measurements. Subject 3 from the older group was uncomfortable due to overweight and thoracic kyphosis, and showed motion artifacts in all acquisitions and was replaced with a ninth subject (mean age after replacement 63 (range, 48–81) years, 4 males, 4 females). In both Subject 5 and Subject 7 from the older group, one of the acquisitions had to be repeated because of motion artifacts.

Figure 6 shows the Bland-Altman analyses for test-retest agreement with and without repositioning. The coefficients of repeatability for  $V_{\text{mean}}$ , PI, and  $N_{\text{detected}}$  were comparable between the repetitions without repositioning and with repositioning, respectively: 0.21 and 0.18 cm/s for  $V_{\text{mean}}$  (equaling 40 and 35% of measured  $V_{\text{mean}}$ ), 0.21 and 0.14 for PI (equaling 50 and 33% of

measured PI), and 66 and 66 for  $N_{\text{detected}}$  (equaling 97% of measured  $N_{\text{detected}}$ ).

Figure 7 shows the differences in  $V_{\text{mean}}$ , PI, and  $N_{\text{detected}}$  between the two age groups. The  $V_{\text{mean}}$ , PI, and  $N_{\text{detected}}$  were lower in the older group compared with the younger group from the TFE experiment (mean age 26 (range, 23–30) years, 4 males, 3 females), but these differences were not significant when comparing these small groups:  $V_{\text{mean}} = 0.42$  versus 0.51 cm/s (effect size = 0.9 ( $P = 0.05$ )),  $PI = 0.41$  versus 0.42 (effect size = 0.1 ( $P = 0.40$ )), and  $N_{\text{detected}} = 68$  versus 91 (effect size = 0.7 ( $P = 0.11$ )).

Simulations

Simulations confirmed that applying a TONE pulse decreases blood signal saturation, and thereby also decreases velocity underestimation, as shown in Supporting Figure S1. Simulations also showed that improved temporal resolution directly decreased the underestimation of the PI approximately linearly, and



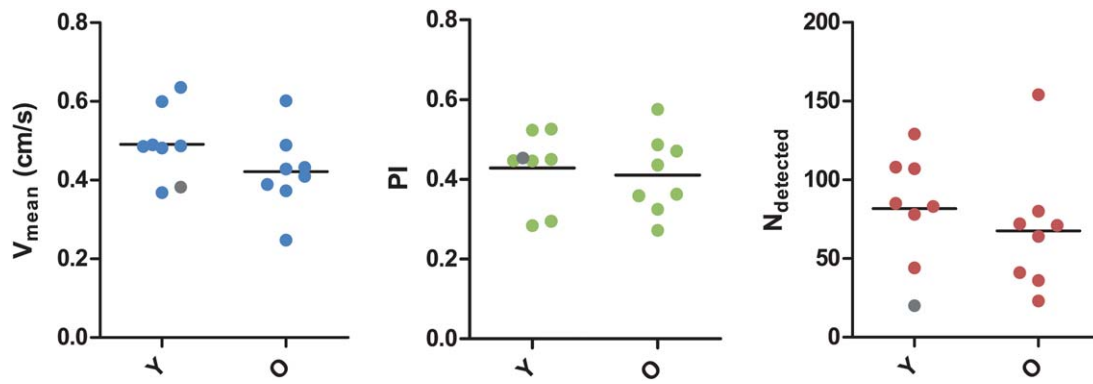


FIG. 7. Age comparison. The colored markers indicate individual subjects, and the horizontal lines show group averages. The graphs compare  $V_{\text{mean}}$  (left graph), PI (center graph), and  $N_{\text{detected}}$  (right graph) between the younger (Y) and older (O) subjects. The excluded subject from the TFE experiment is shown in gray.

indirectly causes the PI to be less dependent on trigger delay, as shown in Supporting Figure S2. For more detailed results, we refer to the Supporting Information.

## DISCUSSION

In this study, 7T 2D Qflow was optimized for the small dimensions and slow-flowing blood found in CSO perforators, which was faster than the previous version, while the temporal resolution was improved (10). In these small vessels, some traditional assumptions in sequence design no longer hold. Applying signal averaging increased the  $\text{SNR}_v$  in perforators only by a fraction of the theoretical increase, whereas it doubled the scan time. Using a TONE pulse significantly decreased the velocity underestimation, which was supported by the simulations. Increasing temporal resolution in turn significantly increased the observed PI (and thus decreased the PI underestimation). Simulations suggested that although decreasing temporal resolution approximately linearly decreases the measured PI, it also worsens the effect of temporal offset on PI. Based on all results, we recommend a protocol using TONE,  $\text{TFE}=2$  (acquired/reconstructed temporal resolution 114/57 ms), and  $\text{NSA}=1$  for future use in patient studies. In a group of older volunteers, the test-retest agreement was found to be twice as good as the previously published version of the method.

Although further increasing the temporal resolution beyond that of the recommended  $\text{TFE}=2$  protocol leads to less PI underestimation, it also yields an impractically long scan time. Longer scan times make the images prone to motion artifacts. With these improvements on the 7T 2D Qflow from the previous publication, assessing velocity pulsation in small vessels with slow-flowing blood, such as the CSO perforators, can be done in a shorter scan time and with improved accuracy. The shorter scan time is beneficial for application in patient studies.

### NSA Experiment

The counter-intuitive result that signal averaging only slightly increased  $\text{SNR}_v$  is presumably caused by motion. It is likely that perforators were averaged with

surrounding tissue as a result of motion and their small dimensions, thus diminishing the gain of signal averaging. One group reported an average motion of 0.4 mm between 3-s volumes (16). During our minutes-long scan, this would likely lead to perforators averaging with tissue, as our in-plane voxel size was 0.3 mm and CSO perforators have diameters between 0.01 and 0.3 mm (17,18). Experimental flaws are unlikely, as background SNR did increase with the expected square root of 2. Because the  $\text{SNR}_v$  increased by such a small amount, the number of detected perforators (with a velocity higher than the noise floor) also increased by only a small amount. The suboptimal gain in  $\text{SNR}_v$  makes signal averaging inefficient in this case. Another common way to increase  $\text{SNR}_v$  is to adapt the  $V_{\text{enc}}$  to the expected velocities. A lower  $V_{\text{enc}}$  could be used, as the average velocities that are measured are much lower than the current  $V_{\text{enc}}$  of 4 cm/s. However, the duty cycle of the gradient system and the considerable peripheral nerve stimulation prevent decreasing the  $V_{\text{enc}}$  further.

### TONE Experiment and Simulation

The measured velocities and  $\text{SNR}_v$  increased significantly when applying the TONE pulse. The increase in measured velocities is likely caused by a decrease of the velocity underestimation. Because of the partial-volume effect, the measured velocities are underestimated. The ratio of blood signal to tissue signal is suboptimal, because blood spins saturate toward the end of the slice. Simulations showed that, as per design, the TONE pulse decreases saturation and increases blood signal. This backs up the interpretation that the observed increase in velocity is in fact a decrease in underestimation. Simulations also showed that smaller vessels would be detectable, because  $\text{SNR}_v$  would increase. This is consistent with the considerably larger number of detected perforators obtained when applying TONE. Although the longer RF pulse for TONE does increase TR and thereby worsens temporal resolution, it only does so by a small amount. The significant decrease in underestimation makes applying the TONE pulse worth this small cost.



### Temporal Resolution Experiment and Simulation

The measured PI increased with improving temporal resolution. This shows that the waveform of CSO perforators contains higher frequencies that are picked up with the higher temporal resolution. It should be noted that the SNR per single image (one cardiac time point) is equal in all acquired temporal resolutions, as they are made in steady state with the same TR and flip angle. Therefore, a difference in observed PI cannot be explained by a difference in noise levels. Although higher temporal resolution improves the measurement of the PI, it also increases scan time significantly. The highest temporal-resolution acquisition in volunteers with low heart rates can reach scan times of over 10 min, which is not practically feasible. Simulations showed that measured PI decreases approximately linearly with temporal resolution. The simulations predicted that the measured PI would approximately decrease with 15% between 57- and 114-ms temporal resolution. The measured decrease between these temporal resolutions was approximately 18%, which shows that measurement and simulation are in agreement. The measured PI becomes more sensitive to trigger delay with lower temporal resolutions. Temporal resolution should be as high as possible for both this reason and for the direct underestimation of PI, but only within a feasible scan time. We feel that the TFE factor = 2 acquisition still has a feasible scan time (shorter than the previously published method). With its improved temporal resolution, this is the best combination of attributes from our experiments.

### Applicability

Now that 7T 2D Qflow is optimized for small vessels, it is possible to assess small vessel function even better, and our current results show that application is also feasible in older subjects. The next step will be to apply the technique in patients with SVD. It is known that large-vessel PI is increased in patients with SVD, and it is hypothesized that this might cause damage at the level of the small vessels (20,21). Previously, the smallest individual vessels that could be imaged individually were the lenticulostriate arteries, which have diameters above 0.3 mm (22). Our previously published method expanded this range to reach CSO perforating arteries (10). With the technique developed in this work, it is possible to better verify whether the PI in SVD patients is also increased at the level of the small vessels, close to the level at which SVD-related tissue damage occurs.

A further improvement of the procedure is the fully automatic processing of velocity data. Manually looking through the flow data for many small vessels could take several hours, whereas processing is now completed in several minutes (with most time spent on segmentation). Besides saving time, it also eliminates subjectivity from the analysis. The improved acquisition detected approximately four times the number of manually detected vessels in the previously published method (10). These improvements together explain that the coefficient of repeatability is twice as good compared with the previous method. It is worth noting that the test-retest agreement was not worse after repositioning of the subject with replanning of the

slice compared with just a directly repeated scan. This implies that thermal noise and physiological noise are the major contributors to the uncertainty in the measurements, and that the method is not sensitive to the planning if the planning is performed in a well-defined way.

The group of older volunteers had lower blood-flow velocities and less detected vessels than younger volunteers. Although these differences were not significant between these small groups, effect sizes were relatively large and in the expected direction. It is quite likely that these effects would be significant with a larger sample size. When calculating which voxels show significant flow, SNR indirectly enforces a velocity limit under which no vessel will be detected. This indicates that when a patient group has lower velocities than another group, still only the (fewer) fastest flowing vessels will be detected, leading to an underestimation of the velocity difference. A more refined detection algorithm that takes the statistical distribution of velocities into account might reduce this underestimation. More refined perforator detection is a challenge for future research.

### Limitations

The three experiments in this work were performed in separate sessions and in separate volunteers, because of scan time and planning limitations. During the NSA and TONE experiments a gradient amplifier and the receive-channel pre-amplifiers of the scanner were replaced. Within experiments, however, conditions did not change, ensuring validity of the results. We reported improvements in the underestimation of velocity and PI, whereas there is no gold standard to supply true values, which is a weakness of this study. However, we are confident in our interpretation, as both observations in the TONE and in the TFE experiment were backed up by simulations. When taking into account an inherent underestimation of the measured velocities, our measurements also approximately agree to known blood-flow velocities in human retina arterioles, which have comparable diameters (11). For the NSA experiment we performed two NSA = 1 repeats and combined them into a single NSA = 2 repeat. Although this ensures the shortest interval between the NSA = 1 and NSA = 2 acquisitions (and thus the highest possible overlap in detected perforators), it might not have the same blurring effect of a true NSA = 2 acquisition. This depends on the order in which k-lines are acquired and varies per vendor and system setting. However, if the volunteer displaced, the perforators would at least partially be averaged with surrounding tissue in both cases. Three of 33 subjects were excluded from the analysis, which shows that future studies should pay attention to preventing possible causes of subject motion. Although we were able to assess the test-retest agreement both with and without repositioning of the volunteers in the scanner, we did not test the interoperator agreement. However, the intended slice location and orientation is very straightforward, and should not yield much interoperator variability after proper instructions.

The velocity threshold used in automated detection is somewhat arbitrary, because it is based on an estimate of

the noise. This estimate correlates with actual noise, making the threshold consistent between acquisitions and volunteers. In practice, this determines the balance between detecting more vessels and including more noise voxels. In any case, our method detects only the subset of perforators that have the highest flow, like the proverbial tip of the iceberg. Whether this is a true limitation depends on the research question that is targeted while applying this method in patient studies. Nonetheless, hemodynamic changes in the detectable subset of perforators are informative of changes in perforators in general. It should be noted that the number of detected vessels does depend on the SNR and, thus, indirectly on the velocities and diameters of the perforators. Differences in the number of detected perforators among different subjects or patient groups are therefore unlikely to reflect differences in vessel density. They indirectly reflect a difference in hemodynamic status instead.

## CONCLUSIONS

We developed a better, faster 7T 2D Qflow method to assess CSO perforator function. By not using signal averaging, the scan time was halved. Applying a TONE pulse significantly decreased velocity underestimation. Increasing temporal resolution improved PI underestimation, but had to be balanced with increased scan time. The automated perforator detection completely eliminates user input, and thereby decreases subjectivity and processing time. These improvements together have made the repeatability of the acquisition twice as good, even in older subjects. The contribution of this work is a sequence that is optimized for CSO perforators and has a scan time short enough to make it feasible for use in SVD patients. As such, it has the potential to allow non-invasive assessment of small-vessel function in SVD.

## REFERENCES

- Wardlaw JM, Smith C, Dichgans M. Mechanisms of sporadic cerebral small vessel disease: insights from neuroimaging. *Lancet Neurol* 2013;12:483–497.
- Gorelick PB, Scuteri A, Black SE, et al. Vascular contributions to cognitive impairment and dementia: a statement for healthcare professionals from the American Heart Association/American Stroke Association. *Stroke* 2011;42:2672–2713.
- Feldman H, Levy AR, Hsiung GY, et al. A Canadian cohort study of cognitive impairment and related dementias (ACCORD): study methods and baseline results. *Neuroepidemiology* 2003;22:265–274.
- Broderick JP, Brott TG, Kothari R, Miller R, Mills D, Minneci L, Khoury J. Incidence rates of ischemic stroke and stroke subtypes among blacks. *Neurology* 1997;48:7003.
- Sacco S, Marini C, Totaro R, Russo T, Cerone D, Carolei A. A population-based study of the incidence and prognosis of lacunar stroke. *Neurology* 2006;66:1335–1338.
- Chamorro A, Sacco RL, Mohr JP, Foulkes MA, Kase CS, Tatemichi TK, Wolf PA, Price TR, Hier DB. Clinical-computed tomographic correlations of lacunar infarction in the Stroke Data Bank. *Stroke* 1991;22:175–181.
- Sudlow CL, Warlow CP. Comparable studies of the incidence of stroke and its pathological types: results from an international collaboration. *Stroke* 1997;28:491–499.
- Norrving B. Lacunar infarcts: no black holes in the brain are benign. *Pract Neurol* 2008;8:222–228.
- Pantoni L. Cerebral small vessel disease: from pathogenesis and clinical characteristics to therapeutic challenges. *Lancet Neurol* 2010;9:689–701.
- Bouvy WH, Geurts LJ, Kuijff HJ, Luijten PR, Kappelle LJ, Biessels GJ, Zwanenburg JJM. Assessment of blood flow velocity and pulsatility in cerebral perforating arteries with 7-T quantitative flow MRI. *NMR Biomed* 2016;29:1295–1304.
- Tayyari F, Venkataraman ST, Gilmore ED, Wong T, Fisher J, Hudson C. The relationship between retinal vascular reactivity and arteriolar diameter in response to metabolic provocation. *Invest Ophthalmol Vis Sci* 2009;50:4814–4821.
- Atkinson D, Brant-Zawadzki M, Gillan G, Purdy D, Laub G. Improved MR angiography: magnetization transfer suppression with variable flip angle excitation and increased resolution. *Radiology* 1994;190:890–894.
- Eissa A, Wilman AH. Ramped RF excitation in 3D TOF MR angiography at high magnetic field. In *Proceedings of the 12th Annual Meeting of ISMRM, Kyoto, Japan, 2004*. p. 369.
- Dyverfeldt P, Bissell M, Barker AJ, et al. 4D flow cardiovascular magnetic resonance consensus statement. *J Cardiovasc Magn Reson* 2015;17:72.
- Ashburner J, Friston KJ. Unified segmentation. *NeuroImage* 2005;26:839–851.
- Zeng L-L, Wang D, Fox MD, Sabuncu M, Hu D, Ge M, Buckner RL, Liu H. Neurobiological basis of head motion in brain imaging. *Proc Natl Acad Sci U S A* 2014;111:6058–6062.
- Furuta A, Ishii N, Nishihara Y, Horie A. Medullary arteries in aging and dementia. *Stroke* 1991;22:442–446.
- Miao Q, Paloneva T, Tuominen S, Pöyhönen M, Tuisku S, Viitanen M, Kalimo H. Fibrosis and stenosis of the long penetrating cerebral arteries: the cause of the white matter pathology in cerebral autosomal dominant arteriopathy with subcortical infarcts and leukoencephalopathy. *Brain Pathol* 2004;14:358–364.
- Glover GH, Li TQ, Ress D. Image-based method for retrospective correction of physiological motion effects in fMRI: RETROICOR. *Magn Reson Med* 2000;44:162–167.
- Mitchell GF, Van Buchem MA, Sigurdsson S, et al. Arterial stiffness, pressure and flow pulsatility and brain structure and function: the age, gene/environment susceptibility. Reykjavik study. *Brain* 2011;134:3398–3407.
- Mitchell GF, Vita JA, Larson MG, Parise H, Keyes MJ, Warner E, Vasan RS, Levy D, Benjamin EJ. Cross-sectional relations of peripheral microvascular function, cardiovascular disease risk factors, and aortic stiffness: the Framingham Heart Study. *Circulation* 2005;112:3722–3728.
- Kang CK, Park CA, Lee DS, Lee YB, Park CW, Kim YB, Cho ZH. Velocity measurement of microvessels using phase-contrast magnetic resonance angiography at 7 T MRI. *Magn Reson Med* 2016;75:1640–1646.

## SUPPORTING INFORMATION

Additional Supporting Information may be found in the online version of this article

**Fig. S1.** TONE simulation results. **a:** Simulation of measured velocities for a range of combinations of vessel diameter and blood flow velocity. The color code denotes measured velocity when applying a TONE pulse. The solid white line shows the left border of combinations of diameter and velocity for which the measured velocity would be significantly above the noise level. The dashed line shows the border of combinations that would be significant when a standard excitation pulse is used (equal to the previously published method (1)). **b:** The iso-velocity contours that are measured when applying a TONE pulse (solid lines) compared with the previously published method (dashed lines).

**Fig. S2.** Temporal resolution simulation results. **a:** The process of simulating a temporal resolution of 114 ms with no added offset. The average curve over volunteers (green markers) is interpolated (dark green line), convolved with a 114-ms rectangular kernel (dark red line) and subsampled to nine samples (red markers). Adding an offset would correspond to the red markers sliding along the dark red line, decreasing the measured peak velocity as the peak sample moves away from the true peak, until the next sample moves closer to the true peak. **b:** The underestimation of PI, which is color coded, as a function of temporal resolution and offset. A value of 100% signifies no underestimation compared with the reconstructed 32-ms temporal resolution. **c:** The average underestimation of PI for the simulated parameters.